

A Coupled Two-Domain Approach for Transpiration Cooling



Valentina König, Michael Rom, and Siegfried Müller

Abstract Transpiration cooling is an innovative cooling concept where a coolant is injected through a porous ceramic matrix composite (CMC) material into a hot gas flow. This setting is modeled by a two-domain approach coupling two models for the hot gas domain and the porous medium to each other by coupling conditions imposed at the interface. For this purpose, appropriate coupling conditions, in particular accounting for local mass injection, are developed. To verify the feasibility of the two-domain approach numerical simulations in 3D are performed for two different application scenarios: a subsonic thrust chamber and a supersonic nozzle.

1 Motivation

In order to bring higher loads into orbit, rocket engines have to be designed with significantly higher thrust. Such engines will experience high thermal loads. In this context transpiration cooling is an innovative cooling concept that gained attention with the development of carbon fiber materials. The general setup is the orthogonal injection of a cooling gas through a porous material. The advantage of this concept is twofold: The porous wall is cooled down by convection energy within the wall while the coolant passes through it. The second cooling mechanism is the development of a cooling film at the interface of the porous sample. This cooling film thickens the incoming boundary layer leading to a reduction of the heat flux at the wall.

V. König · M. Rom · S. Müller (✉)
IGPM, RWTH Aachen University, Templergraben 55, Aachen 52056, Germany
e-mail: mueller@igpm.rwth-aachen.de

V. König
e-mail: koenig@igpm.rwth-aachen.de

M. Rom
e-mail: rom@igpm.rwth-aachen.de

In the 1950s Eckert and Livingood [7] identified the superior characteristics of this active cooling technique. Terry and Caras [27] summarized the possibilities of applying these to rocket nozzles. Transpiration cooling experiments for metallic nozzle applications were performed in [13] and numerical simulations for metallic nozzles can be found in [18].

The development of light-weight permeable high-temperature fiber ceramics, in particular composite carbon/carbon (C/C) materials, investigated for instance by Selzer et al. [26], led to increased interest in transpiration cooling. Transpiration cooled thrust chambers were investigated by Ortelt et al. [24] or Herbertz and Selzer [10]. Experiments in a subsonic hot gas channel were performed by Langener et al. [19]. Additive manufactured porous plates for transpiration cooling applications were recently analyzed in [11].

Numerical simulations of subsonic hot gas channel flow exposed to transpiration cooling were conducted by Jiang et al. [12] and more recently by Liu et al. [20]. Non-uniform injection was investigated by Wu et al. [31]. In Yang et al. [34] each injection channel is simulated separately. In [28] the coupling with a fully resolved pore-network for low Reynolds numbers without heat transfer is used to investigate the effect at the hot gas interface. A monolithic approach for a laminar hot gas flow with a resolved porous medium is presented in [33].

In [4] we developed a two-domain approach where two solvers for the hot gas flow and the porous medium flow are solved in alternation. Data between those solvers are exchanged at the coupling interface. Originally the development of appropriate coupling conditions focused on uniform mass injection [6]. These are modified in [17] to account also for non-uniform mass injection.

In the present work we report on the latest changes on the design of the coupling conditions. Furthermore, we perform numerical simulations for two different application scenarios for transpiration cooling: a subsonic thrust chamber and a supersonic nozzle. For the first scenario we investigate the influence of non-uniform mass injection on the cooling film, whereas for the second scenario the challenge lies in the extension of the range of application.

We first summarize in Sect. 2 the models of the two-domain approach. In particular, the coupling conditions at the interface between the two domains are presented in detail. The numerical methods used are briefly described in Sect. 3. In Sect. 4 numerical results for a subsonic thrust chamber and a supersonic nozzle flow can be found. We conclude with a summary and an outlook in Sect. 5.

2 Mathematical Modeling

For the investigation of transpiration cooling we use a two-domain approach where the flows in the hot gas domain Ω_{HG} and the porous medium domain Ω_{PM} are solved in alternation. At the coupling interface Γ_{Int} boundary conditions for one domain use data from the other domain. Exemplarily, the scenario for a thrust chamber is shown in Fig. 1. Note that the flow in the cooling gas reservoir is not simulated. This model

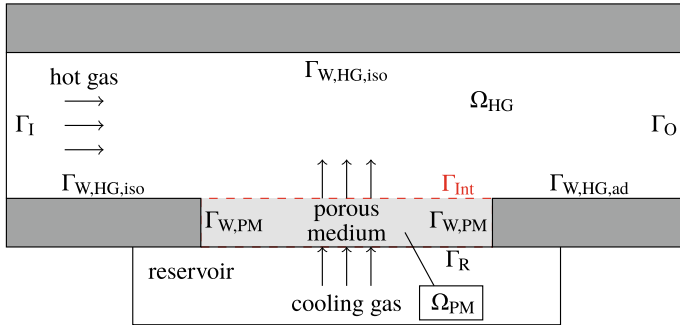


Fig. 1 General transpiration cooling setup

was already presented in detail in previous publications [4, 6, 15]. In the meantime, the coupling conditions have been modified to account also for non-uniform injection. Therefore we focus here on these modifications, see Sect. 2.3, whereas the models in the hot gas domain and the porous medium are only addressed very briefly for the sake of completion, see Sects. 2.1 and 2.2, respectively.

2.1 Hot Gas Domain

The flow in the hot gas domain is assumed to be turbulent. Therefore, we apply a RANS model that formally can be written as

$$\mathcal{L}_{HG}(\mathbf{U}_{HG}) = 0. \quad (1)$$

In our numerical investigations we will consider both the flow in a subsonic thrust chamber at moderate temperatures and a supersonic nozzle at high temperatures. These investigations are motivated by experiments performed in the wind tunnel [19, 25] at University Stuttgart and the detonation-based facility for rocket-engine-like flows [9, 21, 32] at the Shock Wave Laboratory at RWTH Aachen. Therefore, the system (1) of RANS equations will differ for the two scenarios.

Scenario 1: Subsonic thrust chamber. In this scenario the gas is treated as a thermally and calorically perfect gas. The turbulence is modeled by the Wilcox k - ω model [29]. Thus, the system (1) consists of the continuity equation, the momentum equation and the energy equation for density ρ , momentum $\rho \mathbf{v}$ and total energy E as well as two equations for the turbulence kinetic energy k and the specific dissipation rate ω with \mathbf{v} the fluid velocity. The vector of conserved quantities is determined by

$$\mathbf{U}_{HG} = (\rho, \rho \mathbf{v}, \rho E, \rho k, \rho \omega), \quad (2)$$

where the density is Reynolds-averaged and all other quantities are Favre-averaged. The system is closed by an equation of state for a thermally perfect gas. For further details, in particular on the modeling of the Reynolds stress tensor as well as the mean and the turbulent heat flux, we refer to previous work [4, 6, 17]. The following additional quantities enter the model: the specific heat capacity at constant pressure c_p , the dynamic viscosity μ and the turbulent viscosity μ_t , the Prandtl number Pr and the turbulent Prandtl number Pr_t , the specific gas constant R and the isentropic exponent γ .

Scenario 2: Supersonic nozzle. In this scenario the hot gas model has to account for a thermally perfect but calorically imperfect gas mixture of N_s non-reacting species. For this purpose, the RANS equations (1) are extended by additional N_s species equations for the partial densities ρ_α , i.e., the vector of conserved quantities is now determined by

$$\mathbf{U}_{\text{HG}} = (\rho, \rho_1, \dots, \rho_{N_s}, \rho \mathbf{v}, \rho E, \rho k, \rho \omega). \quad (3)$$

Here the turbulent quantities are modeled by Menter's SST k - ω model [22]. The system (1) is closed by an equation of state for a thermally perfect gas mixture. For details we refer to [3, 30].

The system (1) is complemented by suitable boundary conditions for the two scenarios:

Scenario 1: Subsonic thrust chamber. At the inflow boundary Γ_I the Mach number, the density and the temperature are prescribed by $M = M_\infty$, $\rho = \rho_\infty$ and $T = T_\infty$. The turbulence kinetic energy is defined by the turbulent intensity $Tu_\infty = \sqrt{2/3} \overline{k_\infty} / |\mathbf{v}_\infty|$, where \mathbf{v}_∞ is the inflow velocity vector. The turbulent dissipation rate ω_∞ is computed by $\rho_\infty k_\infty / \mu_t$, where the ratio of the turbulent dynamic viscosity to the laminar dynamic viscosity $(\mu_t / \mu)_\infty$ is used in combination with a viscosity curve fit model. At the outflow boundary Γ_O , only the pressure is prescribed by setting $p = p_\infty$. For the walls $\Gamma_{\text{W,HG,iso}}$ of the channel we use isothermal boundary conditions motivated by the thermal wall behavior observed in the experiments in [25]. For the walls $\Gamma_{\text{W,HG,ad}}$ downstream of the porous sample adiabatic boundary conditions account for the changing wall temperature due to the cooling.

Scenario 2: Supersonic nozzle. At the nozzle entry Γ_I we additionally set the mass fractions $X_{\alpha,\infty} = \rho_{\alpha,\infty} / \rho_\infty$ of each species α . At the nozzle exit Γ_O only the outflow pressure is prescribed by setting $p = p_{\text{out}}$. Due to the short test duration of a few milliseconds in the corresponding experiments [9, 21, 32], there is no wall temperature increase. Hence, all nozzle walls are modeled as isothermal walls ($\Gamma_{\text{W,HG,iso}}$).

2.2 Porous Medium Domain

The porous medium flow is characterized by the porosity φ of the material. We assume that the entire void space is connected. Thus, we do not have to deal with

isolated cavities. Furthermore, the porosity is constant in the entire domain. For our two scenarios the flow in the porous medium is laminar. Furthermore, we have to account for the drag that evolves due to the solid obstacle using a Darcy-Forchheimer velocity equation. In short form, the resulting system of equations for a steady state flow reads

$$\mathcal{L}_{\text{PM}}(\mathbf{U}_{\text{PM}}) = 0. \quad (4)$$

It consists of the continuity equation for the density ρ_f of the coolant, the Darcy-Forchheimer equation for the Darcy velocity \mathbf{v}_D and two heat equations for the temperatures T_s and T_f of the solid and the coolant, respectively, i.e.,

$$\mathbf{U}_{\text{PM}} = (\rho_f, \mathbf{v}_D, T_s, T_f). \quad (5)$$

Considering two temperatures allows to account for a potential thermal non-equilibrium of the solid and the fluid. The model is complemented with a perfect gas law for the coolant. Again, we refer to previous work [4] for further details.

The model is supplemented with boundary conditions. Assuming that the conditions in the reservoir are constant and homogeneous we can derive the pressure and the temperatures on the reservoir boundary Γ_R from a fixed coolant temperature T_c , e.g., given by measurements. Furthermore let T_b be the temperature of the solid on the backside of the porous material. Then the boundary conditions on the reservoir boundary Γ_R read $T_s = T_b$, $T_f = T_c$ and $\rho_f = p_R/(R_c T_c)$, where R_c denotes the specific gas constant of the coolant. Furthermore, the solid side walls at $\Gamma_{\text{W,PM}}$ are assumed to be adiabatic, i.e., $\nabla T_s \cdot \mathbf{n} = \nabla T_f \cdot \mathbf{n} = 0$, and the slip conditions to hold, i.e., $\mathbf{n} \cdot \mathbf{v}_D = 0$. Note that at $\Gamma_{\text{W,PM}}$ no boundary conditions for the density ρ_f have to be imposed because viscous effects are neglected in the continuity equation and the Darcy-Forchheimer equation.

2.3 Coupling Conditions

So far we have not yet addressed boundary conditions at the coupling interface Γ_{Int} for the hot gas flow and the porous medium flow. Note that in the present work we only consider injection normal to the porous wall without entrainment of hot gas into the porous medium. At the coupling interface Γ_{Int} the flow quantities \mathbf{U}_{HG} , see (2) or (3), in the hot gas domain Ω_{HG} and \mathbf{U}_{PM} , see (5), in the porous medium domain Ω_{PM} are coupled. Since our model is based on a two-domain approach, we impose boundary conditions for both domains at the interface Γ_{Int} where the boundary conditions for the porous medium domain access data of the hot gas domain (PM \leftarrow HG) and vice versa (HG \leftarrow PM). The coupling conditions, which are specified in the following, make use of the equation of state and the formula for the mass flow rate, in general notation given by $p = \rho RT$ and $\dot{m} = \rho v A$, respectively.

PM \leftarrow **HG**: The coupling conditions at the interface Γ_{Int} for Ω_{PM} use the pressure p_{HG} , the temperature T_{HG} and the temperature gradient ∇T_{HG} of the hot gas at the interface computed from the conservative quantities in \mathbf{U}_{HG} . They are given by

$$v_{D,n} = \frac{\dot{m}_c R_c T_f}{A_c p_{\text{HG}}}, \quad (6)$$

where $v_{D,n} = \mathbf{v}_{D,n} \cdot \mathbf{n}$ denotes the absolute value of the injection velocity vector $\mathbf{v}_{D,n}$ normal to the porous wall with outer unit normal vector \mathbf{n} , \dot{m}_c the prescribed coolant mass flow rate and A_c the surface area of the porous medium, and

$$(1 - \varphi) (\boldsymbol{\kappa}_s \nabla T_s) \cdot \mathbf{n} = c_{p,f} \rho_f v_{D,n} (T_f - T_{\text{HG}}) + \kappa_{\text{HG}} \nabla T_{\text{HG}} \cdot \mathbf{n}. \quad (7)$$

Here $\boldsymbol{\kappa}_s$ and κ_{HG} denote the heat conduction tensor of the solid in the porous medium and the heat conduction coefficient of the hot gas fluid, respectively, and $c_{p,f}$ the heat capacity at constant pressure of the hot gas fluid.

HG \leftarrow **PM**: The coupling conditions at the interface Γ_{Int} for Ω_{HG} use the Darcy velocity normal component $v_{D,n}$ and the fluid temperature T_f of the porous medium at the interface such that

$$\rho = \frac{p_{\text{HG}}}{R_c T_f}, \quad v_n = v_{D,n} \cdot \bar{o}, \quad E = c_v T_f + \frac{1}{2} v_{D,n}^2. \quad (8)$$

In contrast to original work where we investigated **uniform** mass injection [3, 4, 8] we recently added the parameter \bar{o} to account for **non-uniform** injection that is set to 1 for uniform injection. Furthermore, the turbulence kinetic energy k at the interface is set to zero. The specific dissipation rate is determined by

$$\omega = \frac{\rho u_\tau^2}{\mu} \frac{25}{\frac{v_{D,n}}{u_\tau} \left(1 + 5 \frac{v_{D,n}}{u_\tau}\right)}, \quad (9)$$

as proposed by Wilcox [29] to account for mass injection at the modeled porous surface. Here $u_\tau = \sqrt{\tau_w / \rho}$ denotes the friction velocity with the wall shear stress τ_w .

For the supersonic nozzle flow the mass fractions of the coolant $X_{\alpha,c}$ are set at the interface to compute $\rho_\alpha = \rho \cdot X_{\alpha,c}$ with ρ from (8). Note that for foreign gas injection the mass fraction at the interface is 1 for the coolant species and 0 for all species contained in the hot gas flow.

We would like to emphasize that originally in [5] the injection velocity (6) was prescribed to simulate non-uniform injection. For a better control of a specific mass flow rate the parameter \bar{o} representing a local fraction or a percentage of a given mass flow was introduced in [16]. There it was incorporated in the coupling conditions for the porous medium. However, this caused modeling errors in the pressure distribution in the porous medium. Therefore, we recently incorporated this parameter in the coupling conditions for the hot gas [17].

Finally, we emphasize that in the case of uniform injection and thermal equilibrium in the porous material our coupling conditions enforce pressure continuity across the interface. For non-uniform injection and thermal equilibrium the local pressure continuity is lost because of the factor $\bar{\delta}$ in (8), but due to

$$\frac{1}{|\Gamma_{\text{Int}}|} \int_{\Gamma_{\text{Int}}} \bar{\delta} d\gamma = 1 \quad (10)$$

we obtain integral pressure continuity instead. For thermal non-equilibrium, regardless of the injection type, the pressure is not continuous which is in agreement with the literature considering the interface as an idealization of a thin layer in which the pressure can change significantly because of the presence of the porous material [23].

3 Numerical Methods

For the two-domain approach we use two different solvers to discretize the RANS equations (1) and the porous medium model (4).

Porous medium solver. A finite element solver is used to solve the porous medium model. It has been implemented using the deal.II library [1]. For this purpose a weak formulation for the system (4) was derived, see [4, 8]. The resulting system of variational equations is split into two parts:

- a linear elliptic system for the two heat equations to determine the temperatures for the coolant and the solid;
- a nonlinear transport system consisting of the continuity and the Darcy-Forchheimer equation to determine the density of the coolant and the Darcy velocity.

The nonlinear system is linearized and solved by a Newton iteration to which we refer as the inner iteration. The two systems are solved iteratively until the residual of the complete system drops below a chosen tolerance (outer iteration).

Hot gas solver. For the discretization of the RANS equations (1) we use the flow solver Quadflow [2]. This fully adaptive finite volume scheme operates on locally refined B-Spline meshes.

Two-domain solver. For the solution of the coupled problem, we iteratively solve the RANS equations and the porous medium equations for the hot gas flow and the porous medium flow, respectively, by applying the two solvers in alternation and exchanging data at the interface as described in Sect. 2.3. This provides solutions \mathbf{U}_{HG} and \mathbf{U}_{PM} in the two flow regimes. The iterative process is summarized in

Algorithm 1:

- Step 1: Initialize the flow solver.
- Step 2: Transfer data ($p_{\text{HG}}, T_{\text{HG}}, \nabla T_{\text{HG}}$) provided by the flow solver to the porous medium solver.
- Step 3: Converge the porous medium solver.
- Step 4: Transfer data ($v_{D,n}, T_f$) from the porous medium solver to the flow solver.
- Step 5: Converge the flow solver.

In contrast to previous work [4, 6, 8] we use the reservoir pressure p_{R} as a fitting parameter to ensure that the given mass flow rate \dot{m}_c is met at the interface Γ_{Int} and the continuity of the pressure distribution at the interface is established. For this purpose we perform an outer iteration on the flow solver until the target mass flow rate \dot{m}_c is met following [17]. In each iteration i , the mass flow rate \dot{m}_{Int}^i at the interface Γ_{Int} is compared with the given target mass flow rate \dot{m}_c and $p_{\text{R,num}}$ is updated by

$$p_{\text{R,num}}^{i+1} = p_{\text{R,num}}^i + p_{\text{R,num}}^i \cdot \left(1 - \frac{\dot{m}_{\text{Int}}^i}{\dot{m}_c}\right). \quad (11)$$

For an initial guess $p_{\text{R,num}}^0$ we use either experimental data or an approximation determined by the Darcy-Forchheimer equation [16].

4 Numerical Results

In this section we present numerical results for two application scenarios where the two-domain approach is applied to investigate transpiration cooling in a subsonic thrust chamber and a supersonic nozzle.

4.1 Non-uniform Injection into a Subsonic Hot Gas Channel Flow

In the first scenario we investigate non-uniform injection coupling conditions and compare the results with uniform injection. This is motivated by developments in manufacturing allowing to design specific injection patterns of porous materials. This leads to the necessity of affordable non-uniform injection simulations for transpiration cooling. For this purpose, we consider the following configuration: the domains for the porous medium and the hot gas channel are $\Omega_{\text{PM}} = 48 \text{ mm} \times 10.9 \text{ mm} \times 48 \text{ mm}$ and $\Omega_{\text{HG}} = 1, 120 \text{ mm} \times 60 \text{ mm} \times 90 \text{ mm}$, respectively, where the porous medium is mounted to the bottom side of the hot gas channel 580 mm downstream of the channel entrance and centrally in lateral direction. To investigate the influence of the injection pattern on the cooling and, thus, the effectivity of the transpiration

cooling, we consider two injection patterns: the first one depends on the lateral coordinate z and is given by $\bar{\sigma} = 0.887(\sin(\frac{5}{48}\pi \cdot (z + 24)) + 1)$, while the second one depends on the streamwise coordinate x and is given by $\bar{\sigma} = 0.887(\sin(\frac{5}{48}\pi \cdot x) + 1)$. We refer to these as the lateral and the streamwise wave pattern, respectively. For $(x, z) \in [0, 48] \times [-24, 24]$ the wave patterns consist of three peaks and two sinks corresponding to high and low injection rates. The factor 0.887 scales $\bar{\sigma}$ such that (10) holds. A similar pattern was numerically and experimentally investigated in [17] where $\bar{\sigma}$ depends on experimental outflow measurements. The disadvantage of $\bar{\sigma}$ depending on experimental data lies in the necessity to project the discrete data onto the computational mesh.

The porous medium domain is discretized by a mesh with $60 \times 30 \times 60$ cells. The mesh lines are concentrated towards the hot gas and towards the reservoir side by applying a stretching technique.

For the hot gas domain we use a coarse mesh of about 135,000 cells in the first coupling step, i.e., Steps 2–5 of Algorithm 1. Then the data in the hot gas domain are prolonged to a uniformly refined mesh consisting of 1.08 million cells as an initial guess for the solution process on the finer mesh. Another four coupling steps are performed to obtain a converged coupled solution in the hot gas flow domain. Additionally a mesh convergence study was performed with a hot gas mesh of 8.64 million cells.

We perform three computations: uniform injection and non-uniform injection with lateral and streamwise wave pattern. Both the hot gas and the coolant are air. The parameters for the coupled simulations can be found in Table 1.

In Fig. 2 (left) we show the temperature distribution at the wall in the hot gas domain where the porous medium is mounted. In Fig. 2a, b the simulation results for the two non-uniform configurations are presented. We use the same integral mass

Table 1 Flow and porous material parameters for test scenario 1

Flow		Porous material	
Mach number M_∞	0.144	Throughflow direction	Parallel
Inflow temperature T_∞	375.05 K	Porosity φ	12.36 %
Inflow pressure p_∞	88,570 Pa	Solid heat conductivity $\kappa_{s,par}$	15.19 W/(m K)
Isothermal channel wall temp. T_W	362.6 K	Darcy coefficient K_D	$5.98 \cdot 10^{-13} \text{ m}^2$
Integral coolant mass flow rate \dot{m}_c	1.14 g/s	Forchheimer coefficient K_F	$7.86 \cdot 10^{-8} \text{ m}$
Reservoir pressure $p_{R,num}$	216,900 Pa	Volumetric heat transfer coef. h_v	$10^6 \text{ W}/(\text{m}^3 \text{K})$
Coolant reservoir temperature T_c	300.15 K		
Back side temperature T_b	321.45 K		

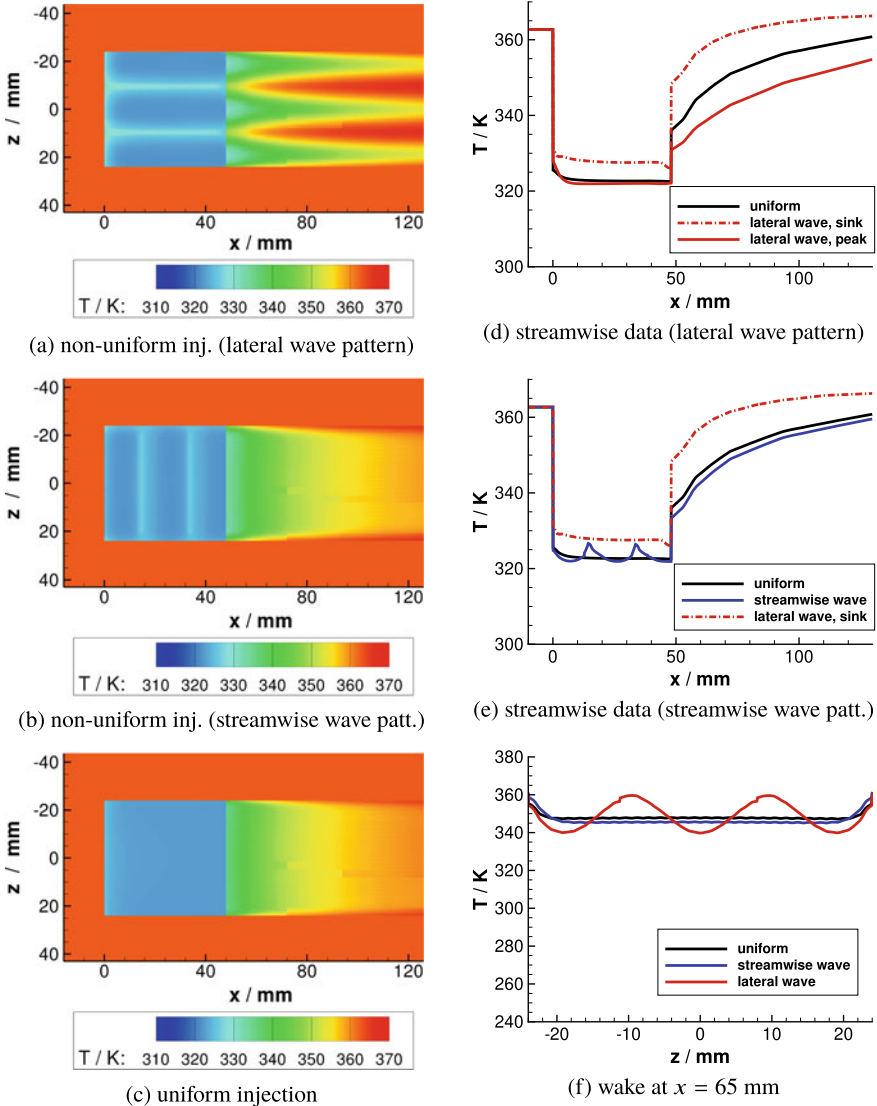


Fig. 2 Comparison of uniform injection and non-uniform injection patterns

flow rate for both the uniform and the non-uniform injection. Therefore, the porous areas with weak injection (light blue on the blowing insert in Fig. 2a, b) are balanced by those with high injection. This has a strong effect on the cooling of the porous material itself and on the wake of the sample.

In Fig. 2a the areas with almost no injection can be seen over the porous material. In the wake of the sample the cooling film exhibits three streaks. The temperatures

in the wake of areas with higher injection are lower than in the uniform injection case. In the wake of areas with almost no injection almost no cooling film is observed leading to high temperatures.

In Fig. 2b the areas with almost no injection can also be seen over the porous material. The cooling film in the wake of the sample is more uniform compared to the lateral wave pattern. The cooling film is slightly extended in streamwise direction compared with the uniform injection case.

To get a better understanding of the cooling film, especially in the wake of the sample, we perform a more detailed investigation by means of temperature data extracted in streamwise direction and lateral to the flow in the wake in Fig. 2 (right). A comparison of the wall temperature for the uniform injection and the lateral wave pattern is presented in Fig. 2d. Temperature data are extracted along the centerline ($z = 0$ mm) for the uniform injection and at a peak ($z = 0$ mm) and at a sink ($z = 14.4$ mm) for the lateral wave pattern. Due to almost no injection at the sink the temperature above the porous material is significantly higher than in the uniform case. It is also significantly higher in the wake ($x > 48$ mm), and at position $x \approx 70$ mm the temperature increases to the isothermal wall temperature $T_W = 362.6$ K. For $x > 70$ mm the temperature is larger than T_W due to the adiabatic boundary condition in the wake of the porous medium and therefore no cooling film can be observed. For the peak the temperatures above the porous material are similar to the uniform injection. In the wake the temperatures are significantly lower due to a thicker cooling film resulting from the higher injection rate.

In Fig. 2e the uniform injection is compared with the streamwise wave pattern along the centerline ($z = 0$ mm). Above the porous material two areas with almost no injection can be identified for the streamwise wave pattern case. Here the temperatures are similar to the temperatures at the sink in the lateral wave pattern case. In the wake of the sample ($x > 48$ mm) the streamwise wave pattern shows a slightly thicker cooling film, probably due to the injection rate peak close to the trailing edge.

In Fig. 2f a comparison of uniform and non-uniform injection temperature data downstream of the sample ($x = 65$ mm) is presented. For the lateral wave pattern three troughs can be observed in the simulations. For the streamwise wave pattern the cooling film is uniform and very similar to the uniform injection. The mean values of the three curves are 348.4, 346.5 and 348.0 K for the lateral wave, streamwise wave and uniform case, respectively.

4.2 Uniform Injection into a Supersonic Nozzle Flow

The second scenario is motivated by the nozzle test facility [9, 21, 32] of the Shock Wave Laboratory at RWTH Aachen. The facility consists of a detonation tube, an attached axisymmetric nozzle, a vacuum tank and a damping section. The detonation tube provides hot water vapor for a quasi-steady nozzle flow for 7–10 ms. In this work, we concentrate on the simulation of the flow in the expansion part of the nozzle which has a length of 340 mm, a throat diameter of 16 mm, a half-opening angle of

15°, a throat radius of curvature of 12 mm and an expansion ratio A_{exit}/A^* of 156. The nozzle has a slot with a length of 110.25 mm and a width of 8 mm in which a porous medium can be installed for transpiration cooling. The leading edge of the slot is positioned about 98 mm behind the nozzle throat (measured on the nozzle centerline).

We perform two simulations with (i) a porous medium with a cross-section surface corresponding to the dimensions of the slot and (ii) a porous medium of the same length but comprising the whole circumference of the nozzle. Due to the short test duration, analogously to the aforementioned isothermal nozzle wall there is no temperature increase of the fluid or the solid temperature in the porous material, i.e., we have $T_f = T_s = T_c$. Hence, for our two simulations the coupling conditions (8) and (9) for the hot gas flow can be directly calculated without simulating the porous medium flow.

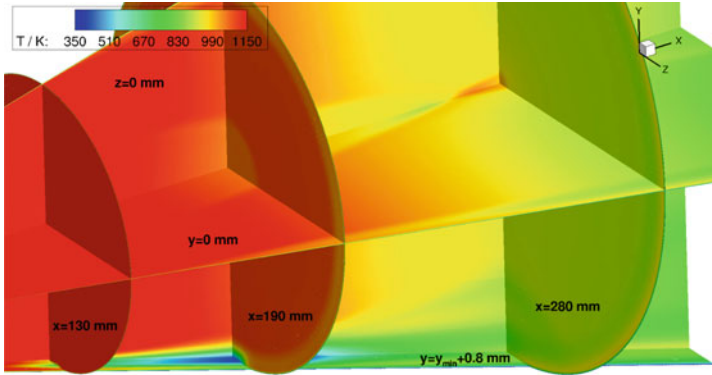
To account for the quasi-steady behavior, we couple the nozzle flow with the calculated porous medium data only once. In particular, we first of all perform a fully adaptive nozzle flow simulation without cooling which provides a final mesh with about 26 million cells. Based on the resulting hot gas data, (8) and (9) are calculated and used as boundary conditions for the subsequent slot and circumferential injection simulations, both with uniform cooling gas injection. These are then conducted by converging the flow solver once more on the final mesh.

The gas in the supersonic nozzle flow is water vapor with initial mass fractions $X_{\text{H},\infty} = 0.00251$, $X_{\text{H}_2,\infty} = 0.01176$, $X_{\text{H}_2\text{O},\infty} = 0.842$, $X_{\text{O},\infty} = 0.01231$, $X_{\text{O}_2,\infty} = 0.08668$ and $X_{\text{OH},\infty} = 0.04474$. The injected cooling gas is helium. The two simulations only differ in the dimensions of the porous medium and are conducted with the parameters listed in Table 2. Note that no parameters regarding the porous material are given because the porous medium flow is not simulated. The flow data are based on experiments planned at the Shock Wave Laboratory for a porous medium with dimensions 110.25 mm \times 8 mm \times 7 mm and characteristics similar to those of the first scenario, see Table 1.

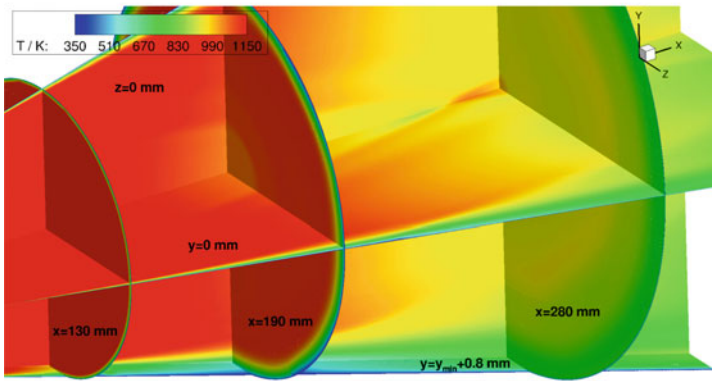
The temperature distribution in the nozzle for slot and circumferential injection can be seen in Fig. 3a and b, respectively, on six slices through the nozzle. The par-

Table 2 Flow parameters for test scenario 2

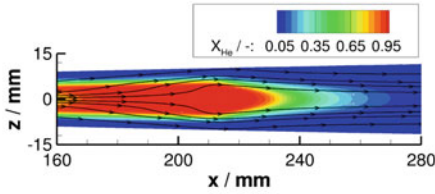
Nozzle flow		Porous medium flow	
Mach number M_∞	1.0	Integral coolant mass flow rate \dot{m}_c	0.58 g/s
Inflow temperature T_∞	3,288 K	Coolant temperature T_c	333.15 K
Inflow pressure p_∞	1.698 MPa	Specific gas constant helium R_c	2,077 J/(kg K)
Outflow pressure p_{out}	1,000 Pa		
Isothermal wall temperature T_W	333.15 K		



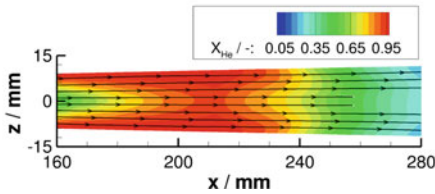
(a) temperature distribution, slot injection



(b) temperature distribution, circumferential injection



(c) streamlines, slot inj. ($y = y_{min} + 0.8$ mm)



(d) streamlines, circ. inj. ($y = y_{min} + 0.8$ mm)

Fig. 3 Comparison of slot and circumferential injection into nozzle flow

ticular positions of the slices are indicated in the figures. Note that only temperatures between 350 K and 1,150 K are displayed. The leading and the trailing edge of the porous medium are positioned at $x \approx 98$ mm and $x \approx 208$ mm, respectively. The formation of a narrow cooling film in the case of slot injection is visible in Fig. 3a, in particular on the slices $x = 190$ mm and $y = y_{\min} + 0.8$ mm, where y_{\min} refers to the local y -coordinate on the nozzle wall at $z = 0$ depending on x . In contrast, in the case of circumferential injection, there is a continuous cooling film on the nozzle wall, see for instance the slices $x = 190$ mm or $y = 0$ mm in Fig. 3b. Since a cooling film is an obstacle to the hot gas flow, a stronger flow deceleration can be observed for the circumferential injection. Hence, the temperatures in the interior of the nozzle away from the walls are slightly higher compared with the slot injection case. This effect is visible in Fig. 3a and b, e.g., on slice $y = 0$ mm between $x = 190$ mm and $x = 280$ mm or on slice $x = 280$ mm.

An interesting phenomenon can be observed when comparing the temperatures in the cooling film boundary layers: With slot injection, lower temperatures can be achieved, as visible around the intersection point of the slices $z = 0$ mm, $y = y_{\min} + 0.8$ mm and $x = 190$ mm. This is probably due to the slot being only a narrow obstacle which can be avoided by the hot gas flow by flowing around it. A comparison of the streamlines on the slice $y = y_{\min} + 0.8$ mm in Fig. 3c, d confirms this conjecture. As a consequence, the slot cooling film can become thicker than the circumferential cooling film and, hence, results in a better cooling effectiveness at selective positions. Figure 3c, d also show the distribution of helium in the nozzle flow. In the slot injection case, the cooling film widens towards the trailing edge of the porous medium at $x \approx 208$ mm and narrows downstream of the trailing edge.

Temperature boundary layer profiles in wall-normal direction in the wake of the porous medium at $x = 280$ mm on the centerline $z = 0$ mm are depicted in Fig. 4a. According to expectations, a better overall cooling is obtained by circumferential injection despite selective lower temperatures achieved by slot injection as described above. However, the comparison with the temperature profile for nozzle flow without any cooling gas injection reveals a significant cooling also in the slot injection case. The temperature peak in the lower part of the boundary layer (wall distance less than 2 mm) is reduced from 945 K (no cooling) to 853 K (slot injection) and 746 K (circumferential injection).

Figure 4b shows the wall heat fluxes for the line $y = y_{\min}$, $z = 0$ mm, which corresponds to the centerline of the slot, with and without cooling gas injection. Due to the isothermal nozzle walls, the wall temperature and the temperature of the cooling gas are the same (333.15 K). Hence, the wall temperature gradients up- and downstream of the leading edge of the porous medium are similar. However, the thermal conductivity of helium is about 3.5 times higher than that of water vapor which leads to the peak of the wall heat fluxes at the leading edge of the injection. Further downstream the heat fluxes rapidly decrease with a value close to zero at the trailing edge of the porous medium in the case of slot injection. The larger wall heat flux over the porous medium for circumferential injection is again explained by the thicker cooling film for slot injection. In the wake of the injection, both heat fluxes slowly increase, but the cooling effect persists up to the nozzle exit.

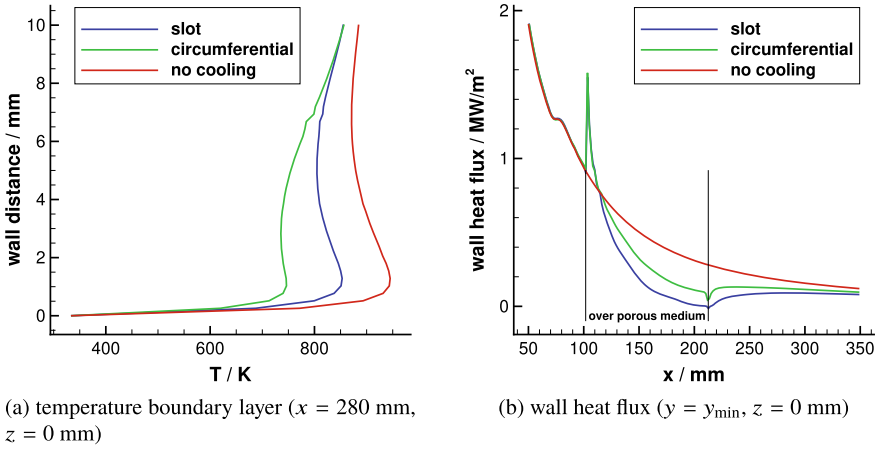


Fig. 4 Temperature boundary layer and wall heat flux for slot and circumferential injection into nozzle flow

5 Conclusion

Transpiration cooling, especially using C/C material, is an active field of research. So far, the heat transfer process of a porous medium flow interacting with a hot gas flow is not yet fully understood. In this paper we presented coupling conditions taking into account non-uniform injection. The numerical results for the subsonic thrust chamber confirm that the injection pattern has a strong influence on the cooling film and therefore needs to be considered in the technical design of a cooling system. This is in accordance with experimental investigations of C/C material characteristics at the DLR Stuttgart and of a wind tunnel setting at the University of Stuttgart in [17] where numerical results are compared with infrared measurements.

The numerical results of cooling gas injection into the nozzle show that our approach is suitable for rocket-engine-like flows even though the porous medium was not simulated in this case. By studying two arrangements of the porous medium (slot or circumferential injection), the simulations led to further insight into the behavior of transpiration cooling. A corresponding experimental study would come at a high cost. Since the experiments at the Shock Wave Laboratory at RWTH Aachen have not yet been conducted, further simulations could help set up the experiments, e.g., by applying different coolant mass flow rates. The experiments will provide data for the wall heat flux on top and in the wake of the porous medium. These will be compared with our numerical results.

So far, the micro-scale behavior of the injection through the porous surface has not been considered. Since a direct simulation is not feasible due to prohibitively high computational costs, effective coupling conditions need to be designed that model the influence of the micro-scale effects on macro-scale quantities, e.g. average of the skin friction coefficient, without resolving the micro-structures. Preliminary work

on this is reported in [14] where an upscaling approach for a porous material surface is developed.

Acknowledgements Financial support has been provided by the German Research Foundation (Deutsche Forschungsgemeinschaft – DFG) in the framework of the Sonderforschungsbereich Transregio 40.

References

1. Bangerth, W., Hartmann, R., Kanschat, G.: deal.II – a general-purpose object-oriented finite element library. *ACM Trans. Math. Softw.* **33**(4), 24/1–24/27 (2007)
2. Bramkamp, F., Lamby, P., Müller, S.: An adaptive multiscale finite volume solver for unsteady and steady state flow computations. *J. Comp. Phys.* **197**(2), 460–490 (2004)
3. Dahmen, W., Gerber, V., Gotzen, T., Müller, S., Rom, M., Windisch, C.: Numerical simulation of transpiration cooling with a mixture of thermally perfect gases. In: *Proceedings of the Jointly Organized WCCM XI - ECCM V - ECFD VI 2014 Congress*, pp. 3012–3023. Barcelona (2014)
4. Dahmen, W., Gotzen, T., Müller, S., Rom, M.: Numerical simulation of transpiration cooling through porous material. *Int. J. Numer. Meth. Fluids* **76**(6), 331–365 (2014)
5. Dahmen, W., König, V., Müller, S., Rom, M.: Numerical investigation of transpiration cooling with uniformly and non-uniformly simulated injection. In: *7th European Conference for Aeronautics and Space Sciences (EUCASS)*. Milan (2017)
6. Dahmen, W., Müller, S., Rom, M., Schweikert, S., Selzer, M., von Wolfersdorf, J.: Numerical boundary layer investigations of transpiration-cooled turbulent channel flow. *Int. J. Heat Mass Transf.* **86**, 90–100 (2015)
7. Eckert, E.R.G., Livingood, J.N.B.: Comparison of effectiveness of convection-, transpiration-, and film-cooling methods with air as coolant. National Advisory Committee for Aeronautics, Report 1182 (1954)
8. Gotzen, T.: Numerical Investigation of Film and Transpiration Cooling. RWTH Aachen University, Diss (2013)
9. Haase, S., Olivier, H.: Influence of condensation on heat flux and pressure measurements in a detonation-based short-duration facility. *Exp. Fluids* **58**, 137 (2017)
10. Herbertz, A., Selzer, M.: Analysis of coolant mass flow requirements for transpiration cooled ceramic thrust chambers. *Trans. JSASS Aerosp. Tech. Japan* **12**(29), 31–39 (2014)
11. Huang, G., Min, Z., Yang, L., Jiang, P.X., Chyu, M.K.: Transpiration cooling for additive manufactured porous plates with partition walls. *Int. J. Heat Mass Transf.* **124**, 1076–1087 (2018)
12. Jiang, P., Yu, L., Sun, J., Wang, J.: Experimental and numerical investigation of convection heat transfer in transpiration cooling. *Appl. Therm. Eng.* **24**, 1271–1289 (2004)
13. Keener, D., Lenertz, J., Bowersox, R., Bowman, J.: Transpiration cooling effects on nozzle heat transfer and performance. *J. Spacecr. Rockets* **32**(6), 981–985 (1995)
14. König, V., Müller, S.: Effective boundary conditions for transpiration cooling applications. IGPM Report 501 (2020). <https://www.igpm.rwth-aachen.de/forschung/preprints/501>
15. König, V., Müller, S., Rom, M.: Numerical investigation of transpiration cooling in supersonic nozzles. In: *8th European Conference for Aeronautics and Space Sciences (EUCASS)*. Madrid (2019)
16. König, V., Rom, M., Müller, S.: Influence of non-uniform injection into a transpiration-cooled turbulent channel flow: a numerical study. In: *2018 AIAA Aerospace Sciences Meeting (AIAA 2018-0504)*. Kissimmee, Florida (2018)
17. König, V., Rom, M., Müller, S., Schweikert, S., Selzer, M., von Wolfersdorf, J.: Numerical and experimental investigation of transpiration cooling with C/C characteristic outflow distributions. *J. Thermophys. Heat Tr.* **33**, 449–461 (2019)

18. Landis, J., Bowman, W.: Numerical study of a transpiration cooled rocket nozzle. In: 32nd Joint Propulsion Conference and Exhibit 2580 (1996)
19. Langener, T., von Wolfersdorf, J., Selzer, M., Hald, H.: Experimental investigations of transpiration cooling applied to C/C material. *Int. J. Therm. Sc.* **54**, 70–81 (2012)
20. Liu, Y., Jiang, P., Xiong, Y., Wang, Y.: Experimental and numerical investigation of transpiration cooling for sintered porous flat plates. *Appl. Therm. Eng.* **50**(1), 997–1007 (2013)
21. Ludescher, S., Olivier, H.: Experimental investigations of film cooling in a conical nozzle under rocket-engine-like flow conditions. *AIAA J.* **57**(3), 1172–1183 (2019)
22. Menter, F.R.: Two-equation eddy-viscosity turbulence models for engineering applications. *AIAA J.* **32**(8), 1598–1605 (1994)
23. Nield, D.A., Bejan, A.: *Convection in Porous Media*, 4th edn. Springer, Berlin (2013)
24. Ortel, M., Hald, H., Herbertz, A., Müller, I.: Advanced design concepts for ceramic thrust chamber components of rocket engines. In: 5th European Conference for Aeronautics and Space Sciences (EUCASS). Munich (2013)
25. Schweikert, S., von Wolfersdorf, J., Selzer, M., Hald, H.: Experimental investigation on velocity and temperature distributions of turbulent cross flow over transpiration cooled C/C wall segments. In: 5th European Conference for Aeronautics and Space Sciences (EUCASS). Munich (2013)
26. Selzer, M., Langener, T., Hald, H., von Wolfersdorf, J.: Production and characterization of porous C/C material. In: Sonderforschungsbereich Transregio 40 – Annual Report 2009 (2009). <https://elib.dlr.de/60899>
27. Terry, J.E., Caras, G.J.: *Transpiration and film cooling of liquid rocket nozzles*. Redstone Scientific Information Center, Redstone Arsenal, Alabama (1966)
28. Weishaupt, K., Joeke-Niasar, V., Helmig, R.: An efficient coupling of free flow and porous media flow using the pore-network modeling approach. *J. Comp. Physics: X* **1**, 100,011 (2019)
29. Wilcox, D.C.: *Turbulence Modeling for CFD*, 3rd edn. DCW Industries Inc. (2006)
30. Windisch, C.: *Efficient Simulation of Thermochemical Nonequilibrium Flows using Highly-Resolved H-Adapted Grids*. RWTH Aachen University, Diss (2014)
31. Wu, N., Wang, J., He, F., Chen, L., Ai, B.: Optimization transpiration cooling of nose cone with non-uniform permeability. *Int. J. Heat Mass Transf.* **127**, 882–891 (2018)
32. Yahiaoui, G., Olivier, H.: Development of a short-duration rocket nozzle flow simulation facility. *AIAA J.* **53**, 2713–2725 (2015)
33. Yang, G., Weigand, B., Terzis, A., Weishaupt, K., Helmig, R.: Numerical simulation of turbulent flow and heat transfer in a three-dimensional channel coupled with flow through porous structures. *Transport Porous Med.* **122**(1), 145–167 (2018)
34. Yang, L., Min, Z., Yue, T., Rao, Y., Chyu, M.K.: High resolution cooling effectiveness reconstruction of transpiration cooling using convolution modeling method. *Int. J. Heat Mass Transf.* **133**, 1134–1144 (2019)

Open Access This chapter is licensed under the terms of the Creative Commons Attribution 4.0 International License (<http://creativecommons.org/licenses/by/4.0/>), which permits use, sharing, adaptation, distribution and reproduction in any medium or format, as long as you give appropriate credit to the original author(s) and the source, provide a link to the Creative Commons license and indicate if changes were made.

The images or other third party material in this chapter are included in the chapter's Creative Commons license, unless indicated otherwise in a credit line to the material. If material is not included in the chapter's Creative Commons license and your intended use is not permitted by statutory regulation or exceeds the permitted use, you will need to obtain permission directly from the copyright holder.

